The Thesis Committee for Siddharth Senthilnathan
Certifies that this is the approved version of the following thesis:

Surface-Coated Silica Nanoparticles for Conformance Control of Buoyancy-Driven CO_2 Flow

APPROVED BY
SUPERVISING COMMITTEE:

Supervisor:

David A. DiCarlo

Hugh Daigle

Surface-Coated Silica Nanoparticles for Conformance Control of Buoyancy-Driven CO_2 Flow

by

Siddharth Senthilnathan, B.S.

Thesis

Presented to the Faculty of the Graduate School of

The University of Texas at Austin

in Partial Fulfillment

of the Requirements

for the Degree of

Master of Science in Engineering

The University of Texas at Austin

August 2017

Acknowledgements

Without the guidance, support, and encouragement of my advisor, Dr. David DiCarlo, this project would not have progressed to the point it has. He has been patient and generous with his time, and always quick to offer advice borne of years of experience. Dr. Hugh Daigle served as my second reader, and his assistance strengthened this thesis.

I am immensely grateful for the help of Dr. Rafael Longoria, who took the time to teach me how to properly conduct petroleum engineering experimental research. His commitment to rigorous scientific inquiry was inspiring, and his witty and generous spirit was greatly appreciated during my time as a graduate student.

I must also acknowledge Daan Thomassen, who came to UT Austin as a visiting scholar from TU Delft in the Netherlands. His theoretical contributions serve as the basis for a significant portion of the work presented here. He and Arjun Ramsunder, my undergraduate research assistant, were excellent companions during corefloods that ran late into the night.

My colleague Lauren Churchwell contributed important ideas that accelerated the progress of my project. Her detail-oriented nature and ability to find common sense solutions were instrumental in pushing the project through technical bottlenecks.

Finally, I would like to thank the Center for Frontiers of Subsurface Energy Security (CFSES), the Cockrell School of Engineering, and the S.P. Yates Fellowship for their financial support over the course of my graduate studies.

Abstract

Surface-Coated Silica Nanoparticles for Conformance Control of Buoyancy-Driven CO_2 Flow

Siddharth Senthilnathan, M.S.E.

The University of Texas at Austin, 2017

Supervisor: David A. DiCarlo

In light of growing concerns over rising atmospheric concentrations of greenhouse gases like carbon dioxide (CO_2), carbon capture and storage (CCS) has been suggested as a means to reduce the rate of net addition of CO_2 to the atmosphere. One potential CCS method involves injecting CO_2 into deep saline aquifers, where they are designed to reside for long periods of time. High-pressure and high-temperature CO_2/brine flow through porous media is the subject of active research, but faithfully recreating the conditions and forces found deep in the subsurface remains a challenge. In particular, the role of buoyant forces in transporting CO_2 must be studied further, since the long-term migration of CO_2 is dominated by buoyancy.

This study consists of two parts. Chapter 1 discusses buoyancy as relevant to the context of CO_2 sequestration and prior methods used to study buoyancy-dominated flow. Four methods to experimentally recreate buoyancy-driven flow in high-pressure corefloods

are presented: “inject low and let rise,” progressive pressure increase, simplified Darcy’s Law, and the Buckley-Leverett approach.

Chapter 2 investigates the potential of using surface-coated silica nanoparticles to improve the conformance of CO_2 during flow through aquifers. The Buckley-Leverett approach is used to determine a single buoyancy-driven flow rate, and a vertical coreflood is conducted using this flow rate. Core-average saturation and pressure drop measurements across the core are measured, and the *in-situ* CO_2 distribution is visualized by taking axial X-ray CT scans of the core during the experiment. The effect of the nanoparticles is studied by conducting the experiment with three different nanoparticle concentrations: 0 wt% (as a control), 0.5 wt%, and 5 wt%.

The addition of 0.5 wt% of nanoparticles (NP) does not markedly improve the conformance of CO_2 when compared to the control. However, at concentrations of 5 wt% NP, steady-state and residual CO_2 saturation increases, sweep efficiency increases, and CO_2 mobility decreases significantly when compared to the control. The lack of effectiveness of the 0.5 wt% formulation may be due to the influence of perpendicular-to-flow bedding layers that are present in the cross-bedded sandstone core used in the experiments. There are mixed indications regarding the suitability of the Buckley-Leverett approach to predicting the buoyancy-driven flow regime.

TABLE OF CONTENTS

List of Tables

List of Figures

CHAPTER 1: METHODS TO EXPERIMENTALLY REPLICATE BUOYANCY-DRIVEN FLOW AT LAB CONDITIONS

1.1 Introduction to Buoyancy-Driven Flow

As efforts to address the challenges of climate change intensify, researchers are increasingly turning to carbon capture and storage (CCS) methods to sequester carbon dioxide (CO_2), an important greenhouse gas. Most other climate change mitigation efforts (such as improving energy efficiency or transitioning to nuclear and renewable energy sources) represent, at best, less carbon intensive alternatives to current practices. CCS, however, is carbon-negative, which gives it the unique ability to balance rapidly growing global energy demand with the need to limit atmospheric CO_2 concentration. To keep atmospheric CO_2 concentration under 450 ppm, a level that some suggest is a tipping point for ocean acidification and deglaciation (McNeil and Matear 2008, Hansen et al. 2008), the UN IPCC predicts that somewhere between 800 and 5630 gigatons of CO_2 will need to be sequestered (IPCC 2005, pg 355). Today's CO_2 capture rate is a small fraction of that, which indicates that a massive expansion of CCS may be needed to avoid dire effects of climate change (Andrew et al. 2015).

One potential destination for captured CO_2 is deep saline aquifers. As the name suggests, these are aquifers (containing brine) which are porous and deep enough to sustain injectivity and securely contain CO_2 for long periods of time. When CO_2 is initially injected into the reservoir from the surface, applied viscous forces drive CO_2 horizontally away

from the wellbore. CO_2 has a lower density than the surrounding brine and as a result buoyancy forces the CO_2 to start migrating upwards.

CO_2 injection is a viscously-dominated process initially, but viscous pressure gradients dissipate approximately as $Ei\ (r^2)$, where Ei is the exponential integral (Mathews and Russell 1967, Lee 2007). When r is large, the term goes to 0, which implies that applied pressure gradients do not propagate into regions of the reservoir far from the wellbore. Furthermore, viscous pressures decay over time once injection is terminated. Thus in regions of the aquifer far away from the wellbore, and at periods of time long after injection has stopped, it can be assumed that viscous forces are negligible and that the only force driving CO_2 flow is buoyancy.

Figure 1 shows the region of the aquifer that contains the flow physics of interest in this study. After injection into the aquifer has terminated, a distinct plume of mobile CO_2 is buoyantly transported upwards. Just above the CO_2 plume is a small region where CO_2 has not yet reached, but the capillary entry pressure configuration is such that this portion of the reservoir will be the next to be invaded by the CO_2 plume. It is within this region, where initial water saturation is 100% just before CO_2 enters, that we expect to find the clearest occurrence of buoyancy-driven flow.

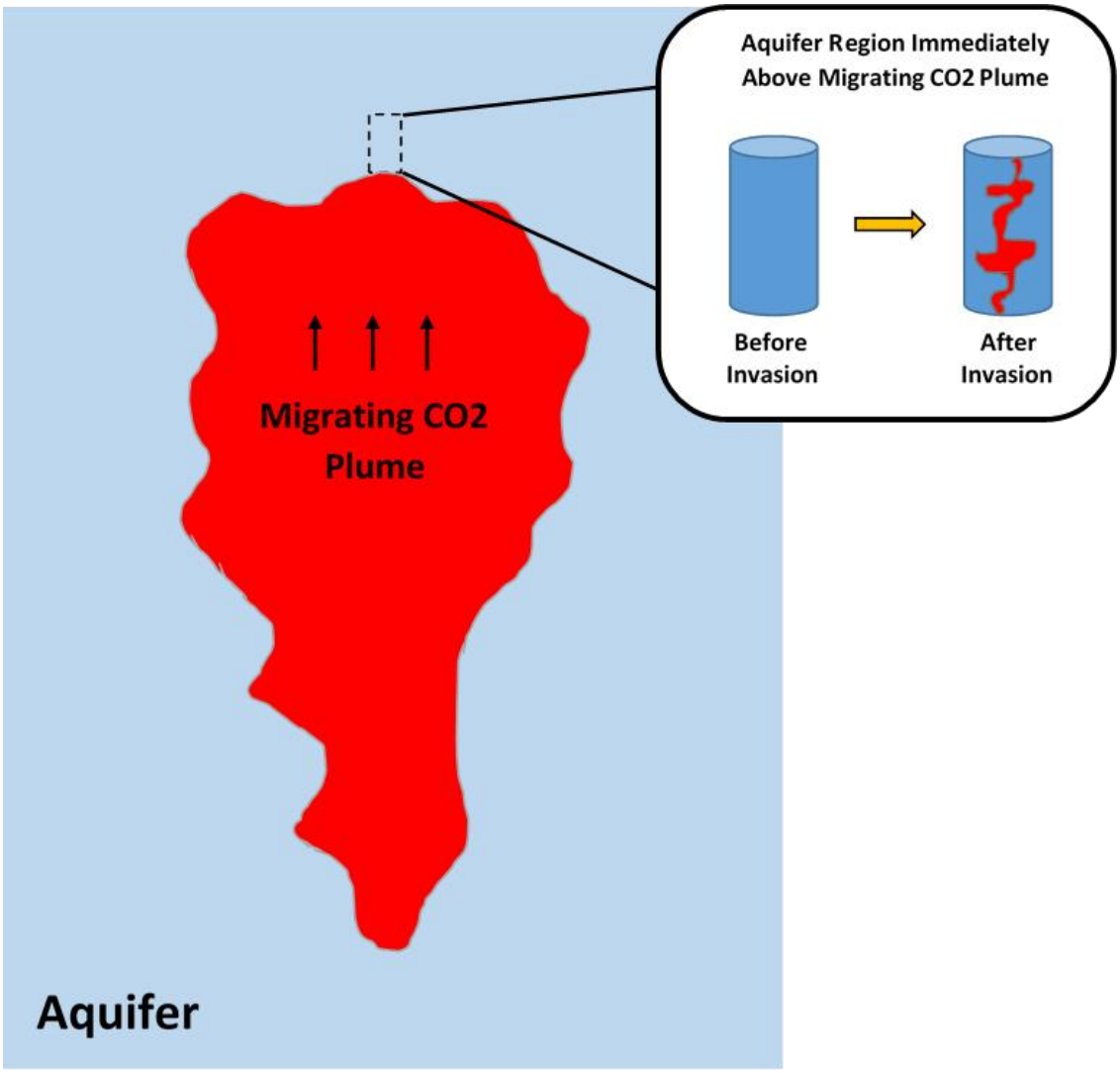

Figure 1. Buoyancy-driven flow occurring in the region that is just about to be invaded by an advancing CO_2 plume.

CO_2 injection into deep saline aquifers is a process that is controlled by the interactions between buoyant and capillary forces. A first-order characterization of this complexity may take the form of computing a dimensionless *Bond number*, Bo:

$$Bo = \frac{\Delta \rho g L}{\sigma / d} \sim \frac{\Delta P_{buoyancy}}{P_{capillary}}$$

where $\Delta\rho$ refers to the density difference between a host fluid and a displacing fluid (brine and CO_2, respectively, in the case of CO_2 injection), g is the acceleration due to Earth's gravity, σ is the interfacial tension between the two fluids, d is the pore/grain diameter, and L is a characteristic length scale. This characteristic length scale depends on the nature of the problem at hand – using a pore diameter as L results in a very small Bond number which indicates that capillary forces dominate at the pore scale. But when L is increased, as it must be when considering core samples or reservoirs, buoyant forces will become comparable to or greater than the capillary forces. The distribution of Bond number throughout a reservoir is highly dependent on the distribution of grain sizes – buoyancy will dominate in some portions of the reservoir ($Bo >> 1$), while in "tight" portions capillary forces will remain dominant ($Bo << 1$). This is the origin of capillary barriers: tight regions of the reservoir hinder buoyant flow until the length scale of the CO_2 accumulation increases enough to raise the Bond number.

Studying buoyancy in the context of carbon sequestration has typically taken one of three forms: field-scale projects, numerical modelling, and lab-scale experiments. Field-scale studies include the Cranfield project in Mississippi, USA and the Sleipner project operated by Statoil in offshore Norway. The Cranfield project injected 5.37 megatons of CO_2 between 2009 and 2015 as part of a study to gauge the feasibility of coupled EOR/CO_2 storage. The researchers attempted to ascertain the long-term storage security of injected CO_2. Although CO_2 leakage into stratigraphic layers above the injection zone was not

detected, it was difficult to measure the effects of buoyancy at such large length scales using traditional field tools (Carrigan et al. 2009).

CO_2 injection has also been taking place at the Sleipner field inn Norway for two decades and the effect of buoyancy on plume development has been demonstrated and studied (Arts et al. 2008). Field-scale studies face the obvious limitation of being time-intensive and expensive to conduct. Furthermore, they are rarely generalizable- the results of one field study reflect the properties of only that field. Analytical solutions for CO_2 plume migration have been developed, but they strongly couple the effect of buoyancy with viscous and dissolution forces (Nordbotten et al. 2005, Saripalli and McGrail 2002).

Numerical models are popular because they can simulate the behavior of buoyant CO_2 under a variety of conditions (Doughty and Pruess 2004, Saadatpoor et al. 2010, Bryant et al. 2006, Krishnamurthy et al. 2017). But these models always balance complexity with physical realism, and geological heterogeneity and multiphase behavior is often difficult to simulate both accurately and efficiently. Researchers at the Cranfield project admitted that their models featured non-unique solutions, and thus important details like CO_2 containment could not be confidently assessed (Hovorka et al. 2013). The predictive capacity of a numerical model depends not only on the formulation of the model itself, but on quality of inputs to that model. While field-scale studies can provide such information, data can more easily be collected by way of lab-scale experiments.

Laboratory studies of buoyancy include investigations of fingering in Hele-Shaw cells (Saffman and Taylor 1958, Fernandez et al. 2002, Maxworthy 1986) and micromodels

(Lenormand et al. 1988, Zhang et al. 2011) which have the advantage of their physics being analytically tractable due to the simplification of flow geometry. Although informative, they too lack the physical realism offered by flow experiments in porous media, such as sand tank experiments (Glass et al. 2000, Fagerlund et al. 2007, Frette et al. 1992, Trevisan et al. 2014, Trevisan et al. 2015). These tanks can be relatively large (on the order of feet), which allows mesoscale flow phenomena to emerge. Additionally, sand placement can be tuned, which allows permeability or porosity distributions to be controlled. However, sand tank experiments can take a long time to conduct (on the order of weeks). Additionally, sand permeability and capillary pressure distributions are either isotropic or artificial (compared to real rocks samples which are naturally heterogeneous). And since sand tank experiments have (to date) been only conducted at low pressures, surrogate fluids must be used in place of high-pressure CO_2 that would be present in true subsurface conditions.

1.2 High-Pressure Corefloods to Study Buoyancy-Driven CO_2 Flow

Corefloods represent a means to achieve those reservoir conditions in the laboratory. Corefloods can reproduce high pressures and temperatures, allowing CO_2 to be used in place of surrogate fluids that cannot simultaneously replicate properties like density, viscosity, miscibility, and surface tension. Although generally smaller than sand tank experiments, corefloods can reveal the true 3D nature of flow in porous media if proper visualization methods are used. Additionally, the cores are easier to clean than sand tanks and turnaround between corefloods is on the order of days. This means that experiments can be repeated under different P-T conditions or with different additives.

High-pressure corefloods, coupled with X-ray CT visualization, have been used to study capillary pressure distributions, CO_2 injection sweep efficiency, residual trapping, and relative permeability (Krevor et al. 2011, Krevor et al. 2012, Chen et al. 2014, Brock and Orr 1991, Catalan et al. 1992). The effectiveness of additives (such as surfactants or nanoparticles) in tuning flow behavior can be easily quantified using high-pressure corefloods with CT scanning (Wellington and Vinegar 1985, Aminzadeh et al. 2012, Wung 2015, Chung 2013)

Although sand tank experiments and simulations/models have been used to study buoyancy-driven flow, very limited work has been done to replicate the particular effects of buoyancy in coreflood experiments. The dearth of such experiments likely reflects their technically challenging nature. Most corefloods involve injecting a fluid at a rate that replicates the interstitial velocities found relatively close to an injection well. But in the case of buoyant flow experiments, CO_2 must instead rise from below the core. Common methods of visualizing *in-situ* fluid flow (like X-ray CT scanning) may be difficult to use in conjunction with the vertically oriented coreflood equipment necessary to produce buoyancy-driven flow. To the best of our knowledge, Wung (2015) represents the only attempt to overcome these challenges. In that study, CO_2 was injected at a rate of 0.8 mL/min into the bottom of a vertically oriented, brine saturated core. The injection rate used in the experiment was based on a Darcy's Law formulation, but it remained unclear how generalizable and reproducible this approach was.

1.3 Potential Methods to Achieve Buoyancy-Driven Flow

The rest of this chapter is dedicated to proposing and analyzing novel techniques designed to mimic the flow of the CO_2 in the upwelling plume depicted in Figure 1. The methods below are categorized as either pressure-controlled or rate-controlled methods. *Pressure-controlled methods* do not deliver fluid to the core at a single rate. Instead, a pressure boundary condition is imposed at the core inlet, which leads to CO_2 movement. The pressure-controlled methods are largely inspired by and are designed to physically replicate previous numerical modelling efforts. *Rate-controlled methods* set a constant flow boundary condition on the inlet face of the core. This is typically how most corefloods are conducted- the operator sets a flow rate that holds for the duration of the experiment.

1.3.1 "Inject Low and Let Rise"

"Inject low and let rise" is a pressure-controlled method inspired by the simulation work of Bryant et al. (2006) in which pure CO_2 is initialized in the lower portion of a reservoir model, and over the course of the simulation the CO_2 migrates upwards under the force of buoyancy alone since no injection is taking pace (Figure 2). The flow patterns of the CO_2 plume are influenced by capillary and permeability heterogeneities, and can lead to fingering and channeling.

One of the key characteristics of this method is that the CO_2 is already within the pore space before any flow begins, and the CO_2 and brine exist in a sharp, shock front-like configuration. The best way to create these initial conditions experimentally is to do the

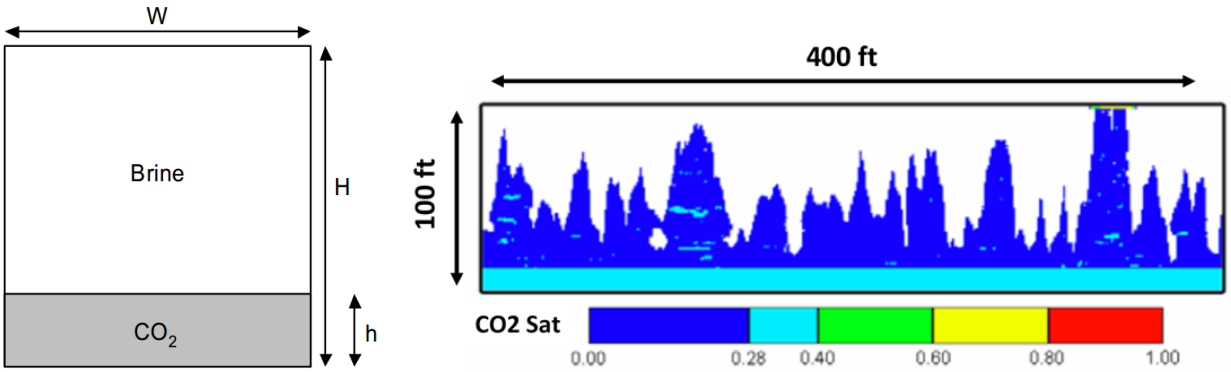

Figure 2. a) Schematic showing the initial conditions of a "inject low and let rise" simulation, in which CO_2 is placed into the lower portion of the reservoir. b) Example of simulation results showing CO_2 fingers created by buoyancy. Adapted from Bryant et al. 2006

following: inject CO_2 at a low flow rate into the *top* of a brine saturated core, shut the inlet and outlet of the core, and then *invert* the core to initiate the CO_2 migration. The initial displacement of brine with less dense CO_2 represents a naturally gravitationally stable system; as long as injection flow rates are low, any perturbations in the CO_2/brine front will decay. Once the desired amount of CO_2 is injected, the core is inverted and the initial shock-like configuration required for "inject low and let rise" will have been achieved.

One potential complication with this method is that the inversion process could itself destabilize the CO_2/brine front. Small perturbations will grow, and the development of particular flow channels will be artificially favored over others. The very act of flipping the core would introduce another variable that must be accounted for when characterizing buoyant fingering behavior. The second issue with the "inject low and let rise method" is the potentially undesired effect of countercurrent flow. In a closed system like that required for an "inject low and let rise" experiment, as CO_2 migrates upward, brine moves

downwards as necessitated by the laws of mass conservation. The contact area between the CO_2 and brine phases are characterized by an increased shear force- a phenomenon known as viscous coupling (Li et al. 2005). Scale is a relevant factor here because in medium or large reservoirs (like sand tanks or aquifers), there may be more space around the CO_2 fingers that water can flow down through. This means that the downward intersticial water velocity will be relatively small- the flow patterns that form in these cases may be natural and minimally affected by viscous coupling and countercurrent flow. But in the confined area of a core, water has no choice but to flow in close contact with CO_2, in the opposite direction, which makes interpreting the resulting flow patterns a more difficult task.

1.3.2 PROGRESSIVE PRESSURE INCREASE

Progressive pressure increase is a pressure-controlled method designed to simulate the interface just ahead of an upwardly advancing CO_2 plume. A vertically oriented core is initially fully saturated with brine and the upstream flow lines are filled with CO_2. Upstream pressure in the CO_2 phase is gradually increased while monitoring flow rate. Once a non-zero flow rate is detected, the pressure is maintained until the CO_2 stops flowing. The pressure is increased again until flow is detected, and the process is repeated until CO_2 breaks through.

Figure 3 portrays the manner in which CO_2 flow rate and applied pressure (as measured by an upstream pump) may evolve over time. The core is held at the initial reservoir pressure P_{res}. The applied pressure on the upstream CO_2 increases until P_{res} is reached. A capillary entry pressure, equal to P_{c1}, must be overcome before CO_2 can enter

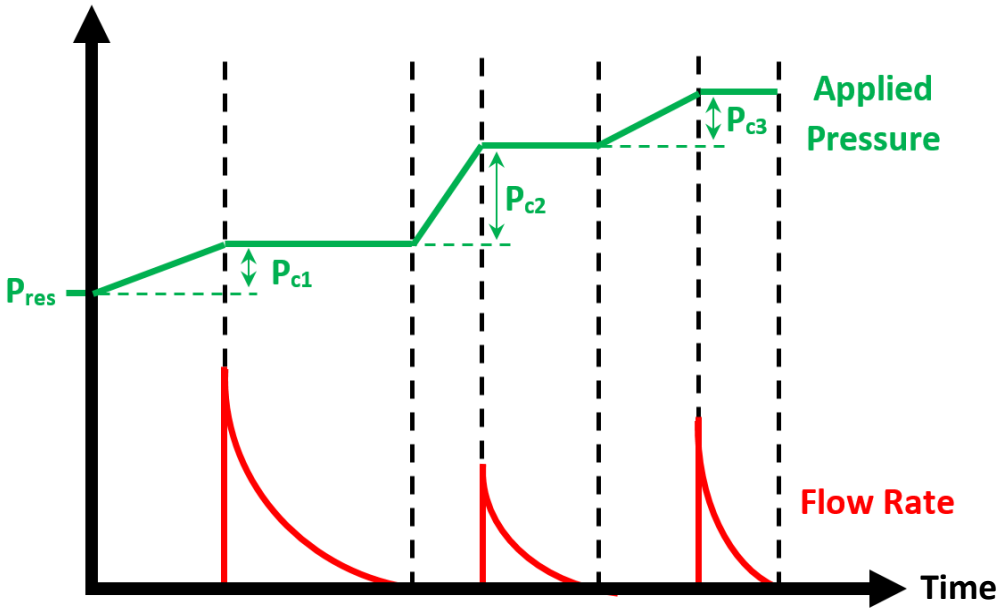

Figure 3. Example of how applied pressure may vary over time in a progressive pressure increase experiment. The transient flows due to the increasing pressure trends are also shown.

the core. Once P_{c1} is reached CO_2 starts to flow and pressure is held constant until flow terminates. The pressure is then increased until it overcomes the next capillary entry pressure threshold, and so on. This method is analogous to mercury injection experiments used to construct capillary pressure curves (Purcell 1949), except the pressure increments end once breakthrough occurs; any further applied pressure increases would result in unwanted viscous gradients.

The progressive pressure increase method also imitates the numerical invasion percolation (IP) models used to simulate buoyancy-driven flow (Wilkinson and Willemsen 1983, Carruthers 2003, Meckel et al. 2015). IP models start with a stochastically generated 3D field of pores, and CO_2 is injected from the bottom of the reservoir. The CO_2 plume

invades until its buoyancy can no longer overcome the capillary threshold pressures of the surrounding pore throats. Pressure is increased until the fluid is mobilized, or until the CO_2 has percolated to the outlet. This method of simulation is computationally efficient because it does not need to model the full range of physics associated with Darcy flow and viscous gradients in porous media. Additionally, time is not a variable that is taken into consideration in IP models- whether a pore is invaded or not depends only on the threshold pressure of that pore and the CO_2 injection pressure.

The progressive pressure increase method may be more difficult to conduct than the "inject low and let rise" and the rate-controlled methods to be discussed below. It requires a pump that can quickly and finely respond to potentially minute changes in flow rate. Automated pump controls are required to achieve these fast response times. The process becomes more difficult when using highly heterogeneous cores because capillary entry pressures are more widely distributed. A large number of pressure plateaus as seen in Figure 3 will be encountered, which makes the duration of such experiments difficult to predict. Additionally, conventional methods of controlling reservoir pressure, such as using nitrogen-charged back pressure regulators (BPRs), may prove to be insufficient. The dome pressure must be set exactly, and pressure fluctuations due to CO_2 flow and expansion at the outlet will likely be larger in magnitude than the typical capillary entry pressures.

1.3.3 Simplified Darcy's Law

Due to the difficulties of implementing these pressure-controlled methods, rate-controlled methods are instead considered. Although perhaps less faithful to the pore-scale physics of buoyancy-driven flow, rate-controlled methods are easier to execute once a buoyancy-driven flow rate, q_b, is determined analytically. As long as the injection rate is less than q_b, it is assumed that buoyancy-driven flow has been achieved or at least well-approximated.

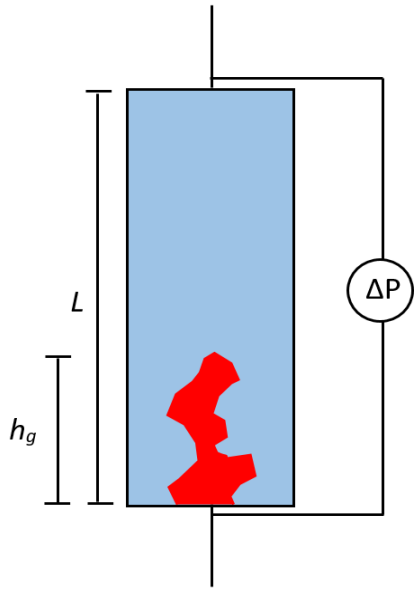

Figure 4. Diagram of CO_2 invading a brine saturated core. Pressure drop across the core is measured using a pressure transducer.

Figure 4 shows the configuration of CO_2 within the core during injection and before breakthrough. The difference in pressure between the upstream and downstream ends of the core is measured with a transducer. This pressure difference can be expressed as the sum of contributions from gravitational/buoyant forces, capillary pressure (due to the

upstream end of the pressure transducer sharing an interface with CO_2 while the downstream end does not), and viscous flow gradients:

$$\Delta P = \Delta\rho g h_c + P_c + \Delta P_{flow}$$

The viscous flow gradient can be further split up into gradients within the CO_2 phase and within the water phase. The pressure drop due to flow can be expressed in terms of a flow rate using Darcy's law:

$$\Delta P_{flow} = \Delta P_w + \Delta P_{CO2} = \frac{q_b \mu_w (L - h_c)}{A k k_{rw}} + \frac{q_b \mu_c h_c}{A k k_{rc}}$$

Where q_b is the buoyancy-driven flow rate, μ_w is the dynamic viscosity of water, μ_c is the dynamic viscosity of CO_2, h_c is the height of the invading CO_2 column, L the the length of the core, A is the cross-sectional area, k is the absolute permeability, and k_{rw} and k_{rc} are relative permeabilities to water and CO_2, respectively.

Dividing the flow gradient into a distinct water and CO_2 contribution requires the assumption that the CO_2 moves as a sharp shock front. Behind the shock only CO_2 moves, and ahead of the shock only water is mobile. We also must make a 1D assumption: both CO_2 and water have constant flow areas equal to the cross-sectional area of the core. Additionally, the relative permeabilities, which generally are a function of saturation, are limited to just a few possible values. All CO_2 within the core exists at its connate water relative permeability, so $k_{rc} = k_{rc,cw}$; all water downstream of the shock front exists at its initial saturation, so $S_w = 1$ and $k_{rw} = 1$; and all water upstream of the shock front exists at

its residual saturation, so $S_w = 1 - S_{g,shock} = S_{w,irr}$ and $k_{rw} = k_{rw}$'. Thus h_c is the only independent variable allowed to vary continuously over the course of the experiment.

Note that the flow rate q_b is the same for both water and CO_2, since displacement is 1-to-1 before breakthrough. In order to minimize the contribution of the viscous flow gradient, we drive the total pressure difference to zero, after which equations (1) and (2) can be combined to solve for the buoyancy-driven flow rate:

$$q_b = \frac{\Delta\rho g h_c + P_c}{\frac{\mu_w(L - h_c)}{Akk_{rw}} + \frac{\mu_c h_c}{Akk_{rc}}}$$

By measuring the capillary entry pressure experimentally and using tabulated relative permeability values for CO_2/brine systems in sandstone (Chen et al. 2014), q_b can be found as a function of the dimensionless invasion depth h_c/L (which in this case is equal to pore volumes injected and average gas saturation), which is shown in Figure 5.

To stay safely within the buoyancy-driven flow regime, a flow rate less than the minimum flow rate shown in Figure 5 should be used- roughly 3 mL/min. It should be noted that this a rather high flow rate that seems unlikely to be seen in the subsurface for buoyant CO_2 plumes. A more realistic estimate for buoyancy-driven flow rate can be arrived at by relaxing some of the simplifying assumptions made above, as we will do when using the Buckley-Leverett approach.

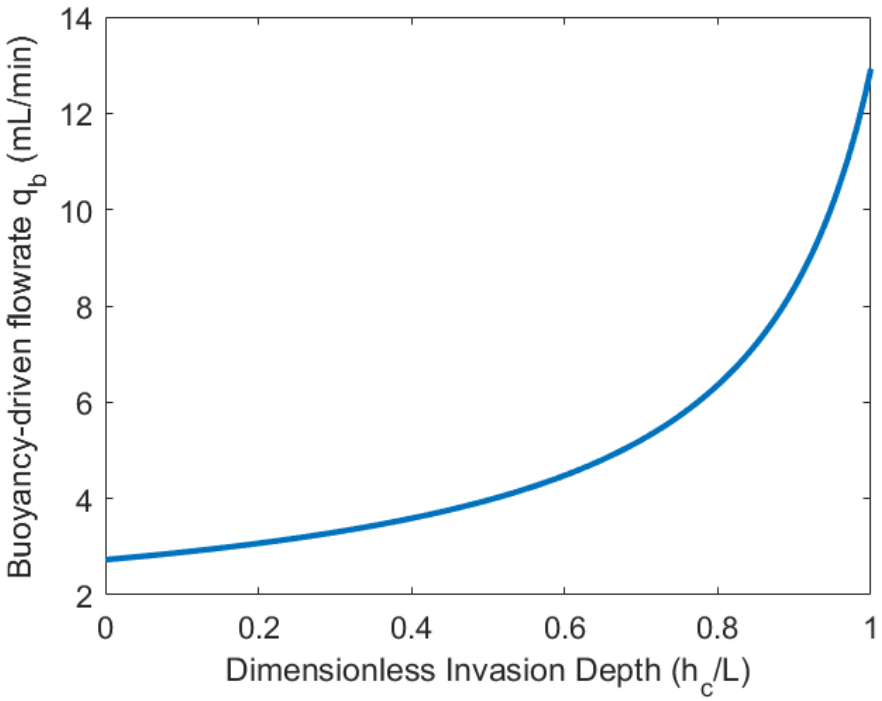

Figure 5. Buoyancy-driven flow rate as a function of dimensionless CO_2 invasion depth.

1.3.4 BUCKLEY-LEVERETT APPROACH

The Buckley-Leverett approach, based on 1D fractional flow solutions (Buckley and Leverett, 1942), was utilized in Krishnamurthy et al. (2017) to calculate a buoyancy-driven flow rate, and is presented in more detail here.

Darcy's Law for buoyancy-driven flow through a vertical column can be expressed as follows (Lake 1989):

$$q_b = \frac{kk_{rc}A}{\mu_c}\Delta\rho g$$

In order to compute q_b, we must first know $k_{r,c}$ (the relative permeability of CO_2) which is a function of S_c (the saturation of CO_2), which is itself a function of q_b. This indicates that the relationship between relative permeability and flow rate must be analyzed iteratively.

The fractional flow equation relates relative permeability to flow rate:

$$f_c = \frac{\lambda_c}{\lambda_c + \lambda_w}(1 - \frac{k\lambda_c A}{q_c}\Delta\rho g)$$

where

$$\lambda_i = \frac{k_{ri}}{\mu_i}$$

and Corey-type relative permeability models incorporate CO_2 saturation:

$$k_{ri} = k_{ri,max}\, S_i^{*n_i} = k_{ri,max}\,(\frac{S_i - S_{i,irr}}{1 - S_{w,irr} - S_{c,irr}})^{n_i}$$

where $k_{ri,max}$ is the endpoint relative permeability of phase *i*, n_i is the Corey exponent, and S_i^* is a mobile phase saturation term. S_i^* is a function of the phase saturation S_i, and the irreducible water and CO_2 saturations $S_{w,irr}$ and $S_{c,irr}$. The Corey exponents and endpoint relative permeabilities are found in Chen et al. (2014).

The workflow is as follows:

1) Choose a range of flow rates.
2) For each flow rate, draw the fractional flow curve (as seen in Figure 6). Note that the fractional flow curve will exceed 1 as a result of gravitational instability due to the vertically oriented core.

3) Draw a tangent line to find the shock saturation. The buoyancy-driven flow rate is that which results in a *total shock*, where the fractional flow at the shock saturation is equal to 1. This implies that the CO_2 saturation within the core will progress as a shock with no rarefaction. In other words, CO_2 saturation will only take one of two values: 0 or S_{shock}. When the shock has progressed to the outlet of the core, the entire core is at steady-state at S_{shock}.

4) Verify that the buoyancy-driven flow rate has been found by setting kri = kri(S_{shcock}) in the Darcy's law equation and evaluating q_b. Figure 6 shows the fractional flow curve for a sample core; when the flow rate is 0.30 mL/min, the buoyancy-driven flow rate is achieved, as indicated by the presence of a total shock.

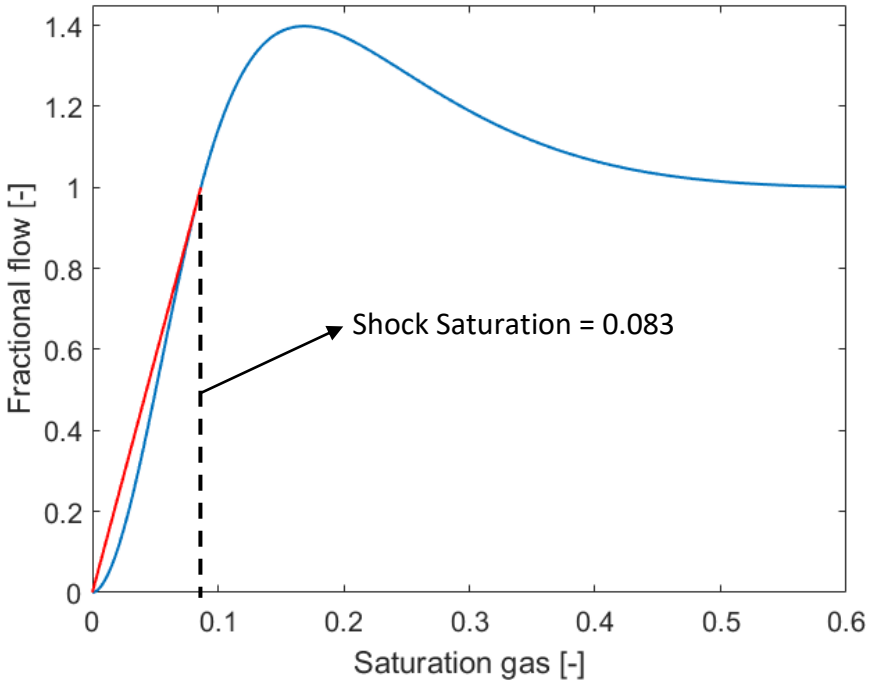

Figure 6. Fractional flow curve at total shock, indicating buoyancy driven flow

The buoyancy-driven flow rate will depend on the particular core used (since permeability and cross-sectional area are inputs to the model). The 0.30 mL/min flow rate was calculated for a sandstone core, and corefloods were performed using that flow rate. Chapter 2 details those experiments. Certain characteristics of buoyancy-driven flow are observed (such as the system reaching steady-state coincident with the breakthrough of CO_2), while others are not (the shock saturation predicted by the Buckley-Leverett analysis was not equal to the experimental saturations). This is likely due to inherently limiting assumptions of the Buckley-Leverett equations, such as core homogeneity and 1D flow.

1.4 Summary of Chapter 1

The characterization of buoyancy-driven flow, particularly of CO_2 through brine, has been an active area of study and will likely grow in importance in the future. Experimentally replicating buoyancy-driven flow conditions has proven to be a challenging task. Previous efforts to study buoyancy-driven flow have mainly come in the form of reservoir-scale projects, numerical modeling, or large lab-scale experiments. There has been limited work on core-scale buoyancy experiments, and fewer still that feature compositionally realistic, high pressure, and high temperature operational conditions like those found in aquifers that would be targeted for CO_2 injection.

Chapter 1 advances four methods to replicate such conditions. Two are broadly termed pressure-controlled methods, which control pressure boundary conditions. The "inject low and let rise" method is simple but the effect of countercurrent water flow may prove to be a confounding variable that detracts from the method's ability to replicate true aquifer conditions. The progressive pressure increase method may offer the highest degree

of fidelity to physically realistic buoyancy-driven flow, but is technically challenging to implement since it requires equipment capable of very fine control. The other two methods are termed rate-controlled methods, wherein a buoyancy-driven flow rate is calculated explicitly and used for CO_2 injection. The simplified Darcy's Law method uses relatively crude approximations to estimate the buoyancy-driven flow rate. The Buckley-Leverett approach relaxes some of these approximations (namely by finding the saturation of the CO_2 shock assumed to be moving through the core). The Buckley-Leverett approach was implemented and the results are shown in the next chapter.

CHAPTER 2: SILICA NANOPARTICLES FOR CONFORMANCE CONTROL OF BUOYANCY-DRIVEN CO_2 FLOW

2.1 Introduction to Nanoparticles for Conformance Control

Conformance control refers to increasing the uniformity with which an injected fluid displaces a host fluid. Better conformance control will result in greater volumetric sweep efficiency and delayed breakthrough, which means that the host fluid has been displaced from a larger portion of the reservoir. Higher sweep efficiency and conformance control is obviously beneficial in commercial EOR projects, but is also important in the context of deep saline aquifer injection of CO_2. There remains uncertainty surrounding the long-term storage security of CO_2 once it has been injected into the subsurface. If the integrity of the overlying caprock is compromised by a high-permeability pathway (such as a fracture), mobile CO_2 could leak through, driven by buoyant forces. Methods that improve conformance control would stop, or at least delay, this type of leakage. One such method is to use emulsions and/or foams stabilized by nanoparticles.

In carbon sequestration applications, a less dense and less viscous fluid (CO_2) is displacing a denser and more viscous fluid (brine). This is a naturally unstable system that leads to gravitationally-driven viscous fingering, and large areas of the aquifer are simply bypassed (Saffman and Taylor 1958, Homsy 1987, Chou et al. 1992, Baker et al. 1999). However, the mobility of CO_2 is significantly reduced when it exists as a foam instead of as a continuous phase. This is due to a variety of factors, including the presence of water lamellae, which block off flow channels and are more resistant to moving through pore constrictions (Hirasaki and Lawson 1985). By blocking flow channels, foam can enter pore

spaces that would otherwise have been bypassed by the bulk fluid. Reducing the mobility of CO_2 is especially important because under reservoir temperature and pressure conditions, CO_2 will exist in its supercritical phase (which has a significantly lower viscosity than liquid CO_2 and is thus more viscously unstable).

Foam can be formed in a variety of ways. *Ex-situ* methods involve mixing or coinjecting the dispersed and continuous phase at high shear rates. These methods do reliably produce foam of desired quality and texture, but field scale deployment would require additional equipment and injection wells may suffer from flow assurance problems. Alternatively, *in-situ* methods for generating foam involve injecting just a single continuous phase and creating the foam within the porous media. This process has been shown to be effective in creating foams, and evidence suggests that the likely mechanism by which this happens is the *snap-off* (Roof 1970). Snap-offs occur when an invading non-wetting fluid forms a curved interface with the host wetting fluid at the pore throat. As fluid accumulates upstream of the interface, the curvature also increases until a critical capillary pressure is reached. Then a bubble of invading fluid snaps off and enters the pore body as a discontinuous phase separated from the upstream pore by a lamella of wetting fluid.

If the foam is able to avoid coalescence to form a continuous phase, it is said to be stable. Foam stability in porous media depends on a wide variety of factors, which reflects a balance between coalescent forces (such as capillary pressure and van der Waals attraction) and dispersive forces (such as double layer repulsion) (Khatib et al. 1998, Derjaguin and Landau 1941). Small solid particles can increase the stability of emulsions

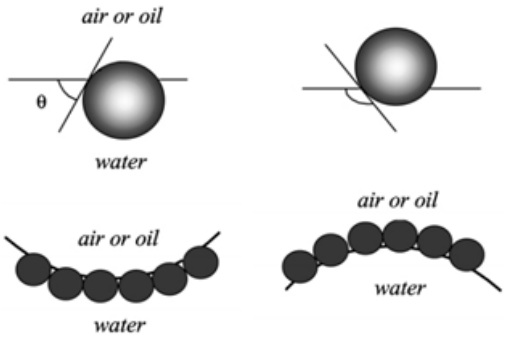

Figure 7. Hydrophilic nanoparticles (on left) and hydrophobic nanoparticles (on right) adsorbed on the interface. Adopted from Binks 2002.

and foams, a fact that has been known for over a century (Pickering 1907, Ramsden 1903). In particular, surface-coated nanoparticles have been featured in numerous recent subsurface applications (Yu et al. 2012, Zhang et al. 2009, Prodanovic et al. 2010, DiCarlo et al. 2011).

Figure 7 shows how nanoparticles are adsorbed onto the interface between the wetting and non-wetting phase (which in our case is CO_2). The surface coating of the nanoparticles can be tuned to create hydrophilic nanoparticles (with $\theta < 90°$) or hydrophobic nanoparticles (with $\theta < 90°$). Nanoparticles stabilize foams primarily through two mechanisms. First, they lower interfacial energy by reducing the contact area between the wetting and non-wetting phases. This increased stability can be expressed as an adsorption energy, which can be on the order of hundreds or thousands of k_BT (Binks 2002). Studies have shown that pore-scale snap-off events can provide this energy to move nanoparticles to the interface (Espinosa et al. 2010). As particle size increases, the interfacial contact area and energy decrease; surfactants (which are often < 1 nm in

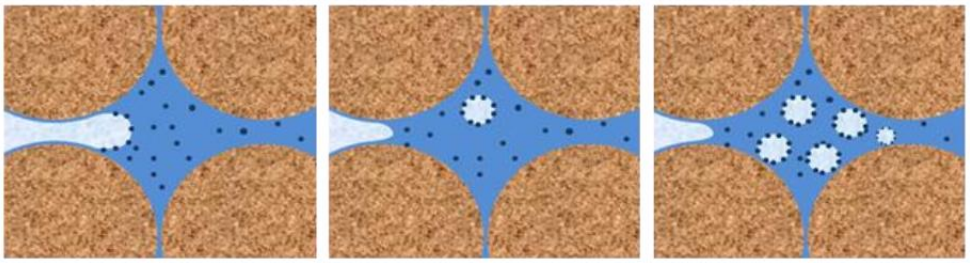

Figure 8. Nanoparticles armor invading non-wetting phase to form droplets that are resistant to coalescence. Adopted from Wung 2015.

diameter) cannot operate by this mechanism and thus may not be robust enough to operate at elevated temperatures.

The second mechanism by which solid particles can stabilize foams is by armoring the interface and sterically hindering bubble coalescence (Tambe and Sharma 1994). Figure 8 shows snap-off events releasing enough energy to overcome the adsorption energy barrier, bringing nanoparticles to the interface. Once at the interface, the nanoparticles repel each other and coalescence is delayed. Upstream capillary forces can eventually become large enough to finally overcome the armoring of the nanoparticles, and then the dispersed bubbles merge to form a continuous phase.

One can begin to consider the change in Bond number under the influence of nanoparticles. When nanoparticles encourage foam formation and endurance, CO_2 is less likely to invade larger pores (with nanoparticle-armored droplets) than it would have been without nanoparticles. This can be viewed as essentially an increase in interfacial tension between brine and CO_2, which increases the capillary entry pressure for larger pores. As a result Bo will decrease in these larger pores that contain nanoparticle-stabilized CO_2 foam. This implies that buoyancy may no longer dominate over capillary forces in those pores,

resulting in mobility loss until the CO_2 plume beneath the pore grows large enough to overcome this capillary barrier.

Krishnamurthy et al. (2017) and Chapter 1 presented a method to experimentally replicate buoyancy-driven flow by using a Buckley-Leverett approach to determine a critical flow rate. That approach was applied in this study, and it was determined that 0.30 mL/min was the critical flow rate for buoyancy-driven flow. Additionally, the potential for nanoparticles to increase flow conformance was studied by saturating a sandstone core with nanoparticle-laden brine into which CO_2 was injected. The corefloods conducted with this particular flow rate make it possible to investigate the interactions between CO_2 plumes and nanoparticles, in the context of long-term buoyant flow.

2.2 Experimental Procedure

2.2.1 Overview of Experimental Setup

Figure 9 shows the experimental setup used for the corefloods. A liquid CO_2 tank at room temperature delivers CO_2 to a series of two accumulators dedicated to holding CO_2. These two 1.5 L accumulators hold enough CO_2 for multiple experiments conducted at 1500 psi. Another 1.5 L accumulator is dedicated to holding brine with varying concentrations of nanoparticles. The polymer-coated silica nanoparticles are provided by Nissan Chemical America Corporation (Version EOR 5XS-V2). The fluids are injected from the accumulators through the core using two Teledyne ISCO 260D syringe pumps operating in continuous flow mode. The core itself is secured inside a core holder that is oriented vertically within a modified medical X-ray computed tomography (CT) scanner

(Universal Systems, model HD-350). The core moves up and down within CT gantry, which makes it possible to investigate the evolution of CO_2 distribution within core during the experiment. A Rosemount 3051S pressure transducer measures the pressure drop across the core. The fluid exits the system via a series of two back pressure regulators (BPRs) manufactured by Core Laboratories (Model BP 100-T-SS). The mass of the effluent fluid is measured using an Acculab scale (Model ALC 1100.2).

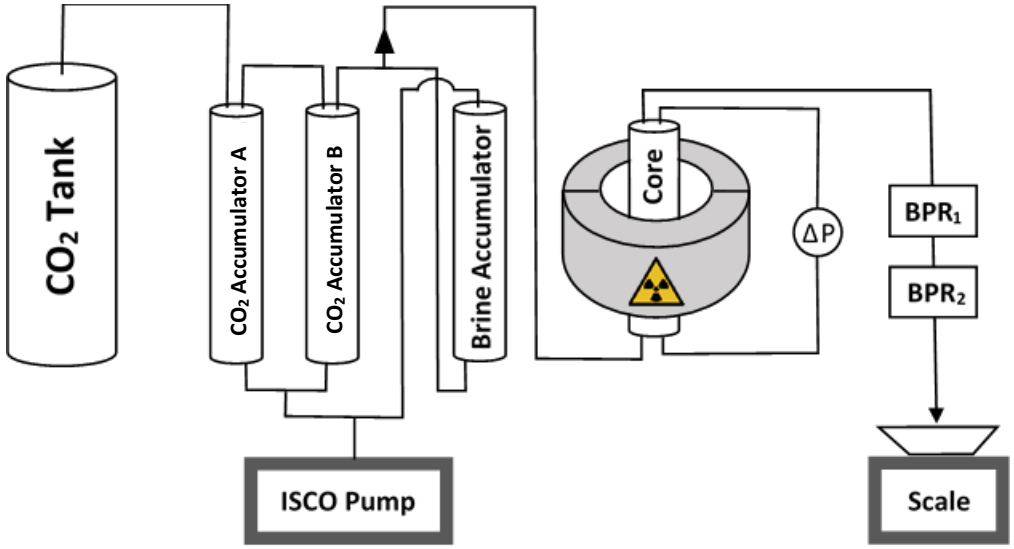

Figure 9. Schematic of experimental setup.

2.2.2 Preparation of Core and Core Holder

An aluminum Hassler-type core holder manufactured by Phoenix Instruments was used for this set of experiments. A highly cross-bedded Boise sandstone core (12” long, 2.85” diameter, permeability = 2.5 Darcy, porosity = 27%) was chosen to replicate the properties of a typical deep saline aquifers. The core was first dried in an oven for 75°C

for 12 hours to remove any residual water saturation. Once the core was dried and cooled, it was shrink-wrapped with Teflon tubing, then surrounded with 5 layers of aluminum foil, then shrink-wrapped again with Teflon tubing. The Teflon layers serve as barriers that are impermeable to water, while the aluminum foil prevents diffusion of CO_2 from the core across into the rubber sleeve of the core holder. This step is important to ensure mass balance. The confining pressure surrounding the core was 2000 psi. The core was then suspended vertically within the CT scanner gantry.

2.2.3 Preparation of Fluids and Initial Saturation of Core

All solutions were prepared with 2 wt% NaCl brine. Two different nanoparticle (NP) concentrations were investigated (5 wt%, and 0.5 wt%) in addition to the control concentration (0 wt%). In order to minimize inter-phase mass transfer across the CO_2/brine interface, the fluids were equilibrated prior to the coreflood. CO_2 accumulator B was filled with approximately 20 mL of 2 wt% NaCl brine before it was filled with liquid CO_2 and pressurized to experimental pressure of 1500 psi. The solubility of CO_2 was determined using data found in literature (Duan and Sun 2003); after incorporating a safety factor, 100 mL of CO_2 was injected into the 1.5 L brine accumulator. The accumulators were maintained at 1500 psi for 12 hours to ensure that the brine and CO_2 reached equilibrium with each other.

Two BPRs were used in the experimental setup. The first BPR dome pressure was set to 1500 psi, which controlled the experimental pressure within the core. The second BPR was submerged in a 55°C heated water bath, and the pressure was set to just above

the vapor pressure of CO_2 at room temperature (approximately 1000 psi). The phase change and expansion that the CO_2 undergoes as it transitions from experimental pressure to atmospheric pressure is a highly endothermic process, which results in water freezing in the flow lines and correspondingly erratic pressure drop readings. The dual BPR/water bath configuration minimized these pressure drop fluctuations. Once the BPRs were in place, the dry core was flushed with non-equilibrated 2 wt% NaCl brine for 1 pore volume (PV). This was followed by 2 PVs of equilibrated brine, after which the core was ready to be injected with CO_2.

2.2.4 FLOODING PROTOCOL AND DATA COLLECTION/PROCESSING

Each coreflood consisted of a drainage process followed by an imbibition. During drainage, CO_2 was injected at a buoyancy-driven flow rate of 0.30 mL/min for approximately 1.2 PVs. The imbibition process consisted of injecting approximately 0.5 PVs of brine at 2 mL/min.

Three streams of data were collected: pressure drop across the core, effluent mass (to determine core-average CO_2 saturation), and matrices containing CT attenuation factors (to determine distribution of CO_2 within the core). Pressure drop data was fed into a LabVIEW system with a sampling interval of 10s.

Mass balance can be used to calculate the overall, core-average CO_2 saturation. Since liquid CO_2 vaporizes at atmospheric pressure and room temperature, the collected effluent contains only water. By closely monitoring the injection rate, elapsed time, and

the volume of fluid in flow lines, one can obtain a core-average CO_2 saturation during drainage and imbibition. Effluent mass was recorded every 15-30 min.

CT data allowed for the visualization of local CO_2 saturation distribution. The core was scanned periodically (one scan sequence every 0.05 PV during drainage and every 0.10 PV during imbibition) to track the changes in saturation over time. Each scan sequence consisted of 30 scans starting at the bottom inlet of the core, with the sample being moved down 1 cm after each scan. Each slice is 1 cm thick, so the scan sequence imaged the entire 30 cm-long core. Scan energy was 140 kV and exposure time was 1 sec.

The CT scanner outputs a 3D matrix of CT attenuation factors, with each element representing CT number averaged over a 0.25 mm x 0.25mm x 1cm voxel. CT numbers can be translated into CO_2 saturations using the following equations:

$$S_{CO_2}(x,y,z) = \frac{CT_{sat}(x,y,z) - CT_{inj}(x,y,z)}{\phi\,(x,y,z) \cdot (CT_{brine} - CT_{CO_2})}$$

$$\phi(x,y,z) = \frac{CT_{sat}(x,y,z) - CT_{dry}(x,y,z)}{CT_{brine} - CT_{air}}$$

where "*(x,y,z)*" is used to explicitly note that some of the terms above correspond to 3D matrices of CT numbers, while other terms are simply scalar values. CT_{sat} is the matrix of CT numbers from the scan sequence of the core when it is completely saturated with brine,

CT_{dry} is the matrix of CT numbers from the scan sequence of a completely dry core, and CT_{sat} is the matrix of CT numbers from a scan sequence taken during the coreflood process. CT_{brine}, CT_{air}, and CT_{CO2} are scalar values representing the CT attenuation factors for 2 wt% NaCl brine, air, and liquid CO_2, respectively. Table 1 contains the reference values for these numbers. Evaluating the equations above yields the porosity distribution (phi) and the CO_2 saturation distribution (S_{CO2}) for a scan sequence. The resulting matrix of CO_2 saturations was passed through a 9-by-9 median filter to reduce data noise.

Table 1. Reference CT Attenuation Factors	
CT_{air}	***-1000***
CT_{brine}	***0***
$CT_{CO2,\ 1500\ psi,\ 293K}$	***-310***

2.3 Experimental Results

2.3.1 Core-Average CO_2 Saturation Data

Figure 10 shows the core-average CO_2 saturation as a function of pore volume injected for each of the three NP concentrations. All experiments were characterized by three saturation regions: a 1-to-1 relationship between PV_{inj} and CO_2 saturation during the drainage process, a plateau corresponding to steady-state CO_2 saturation, and a period of decreasing CO_2 during the imbibition process that ends with CO_2 reaching its residual saturation.

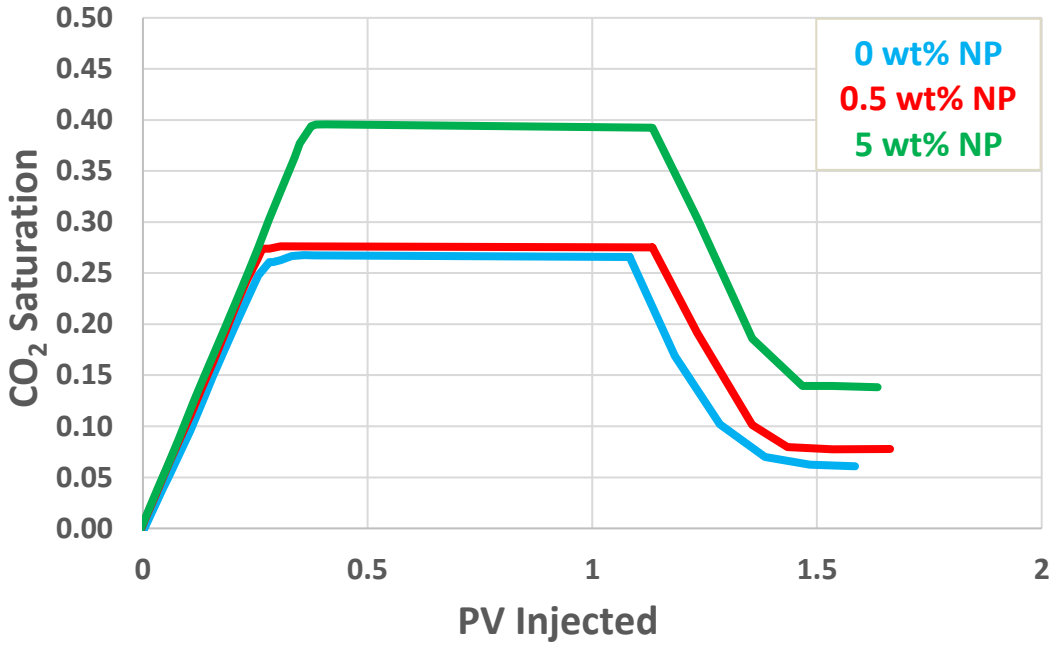

Figure 10: Core-average CO_2 saturation as a function of pore volumes injected during drainage and imbibition.

Table 2 quantifies the key values found in Figure 10. Breakthrough saturation is defined as the saturation at which the curve deviates from straight-line behavior, which corresponds to the moment when CO_2 has made it to the outlet of the core. The trapping ratio is defined here as the ratio of residual CO_2 saturation to steady-state CO_2 saturation.

Table 2: Summary of CO_2 Saturation Data			
	0 wt% NP	**0.5 wt% NP**	**5 wt% NP**
Breakthrough PV (%)	***25***	***27***	***39***
Steady-State Saturation (%)	***27***	***28***	***39***
Residual Saturation (%)	***7***	***8***	***14***
Trapping ratio (%)	***26***	***29***	***36***

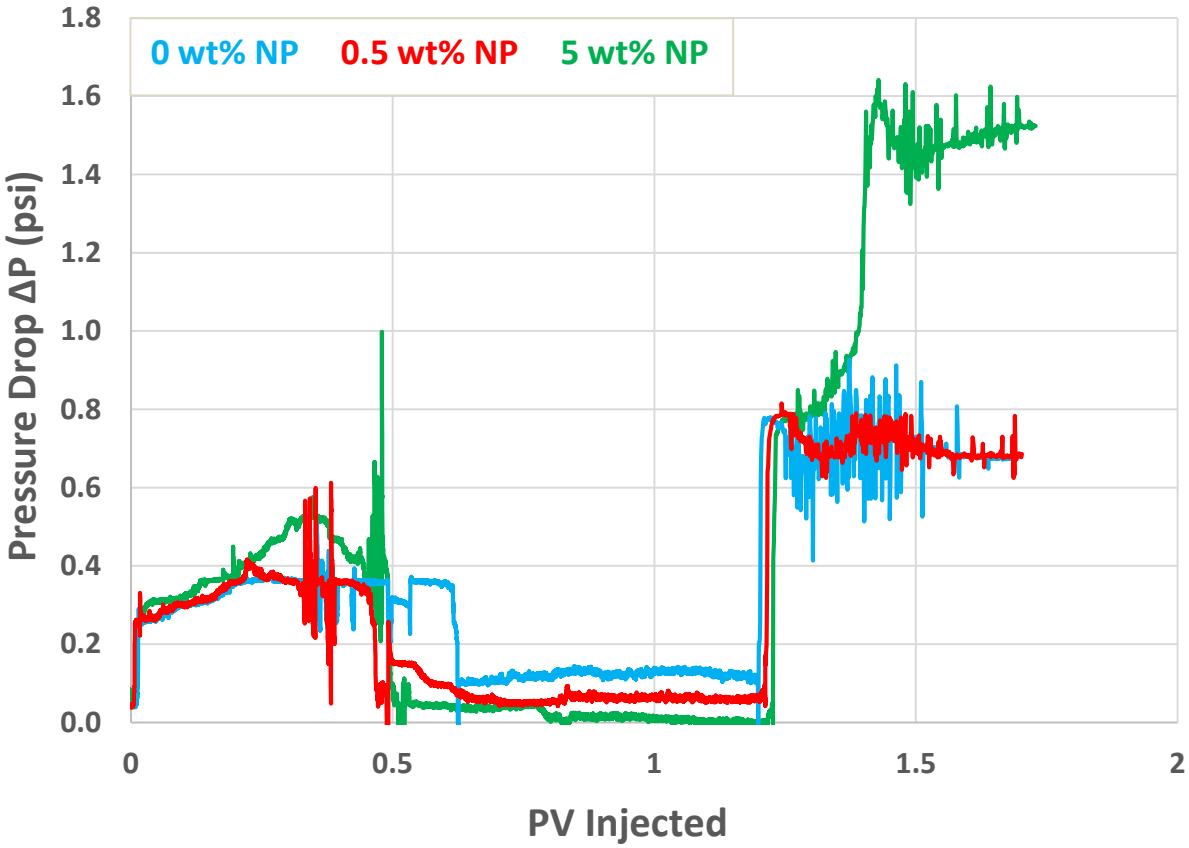

Figure 11: Pressure drop as a function of pore volumes injected during drainage and imbibition.

2.3.2 Pressure Drop (ΔP) Data

Figure 11 shows the pressure drop across the core as function of pore volumes injected for each of the three nanoparticle concentrations. Each ΔP curve begins with a sharp increase to approximately 0.25 psi, which corresponds to the capillary entry pressure for CO_2 invasion into the core. The ΔP then increases to a peak, and then starts to fluctuate due to freezing in the flow lines (as explained in the Methods sections), which is indicative of CO_2 exiting the system. The fluctuations occur after the plateauing of the CO_2 saturation as seen in Figure 10. The ΔP then dives to its steady-state value. There is another sharp

increase in ΔP when the imbibition process begins. The residual ΔP value reached during imbibition is higher than that steady-state ΔP because the flow rate during imbibition is higher than during drainage.

Table 3 lists some of the key values captured in Figure 11. Mobility reduction factor represents the ratio of the peak ΔP to the capillary entry pressure.

Table 3: Summary of ΔP Data			
	0 wt% NP	0.5 wt% NP	5 wt% NP
Peak ΔP (psi)	*0.374*	*0.391*	*0.523*
Mobility Reduction Factor	*1.50*	*1.56*	*2.09*
Steady-state ΔP (psi)	*0.120*	*0.066*	*0.002*
Residual ΔP (psi)	*0.676*	*0.679*	*1.520*

2.3.3 CO_2 Distribution from CT Data

CT data was processed using Equations 1 and 2 and was visualized using several MATLAB scripts. Figure 12 shows the resulting distribution of CO_2 within the core at several points during the drainage experiment. Each row corresponds to a nanoparticle concentration, and each column represents a particular volume of CO_2 injected. The left-hand image of each pair shows the axial (cross-sectional) slices located 1 cm, 4 cm, 7 cm, 10 cm, 13 cm, 16 cm, 19 cm, 22 cm, 25 cm, and 28 cm from the bottom inlet of the core. The right-hand image of each pair shows a pseudo-3D model of the core, with a cutaway that displays the CO_2 preferential flow pathways. In these figures, the cool colors correspond to regions of low CO_2 saturation, and the warmer colors correspond to regions of higher CO_2 saturation.

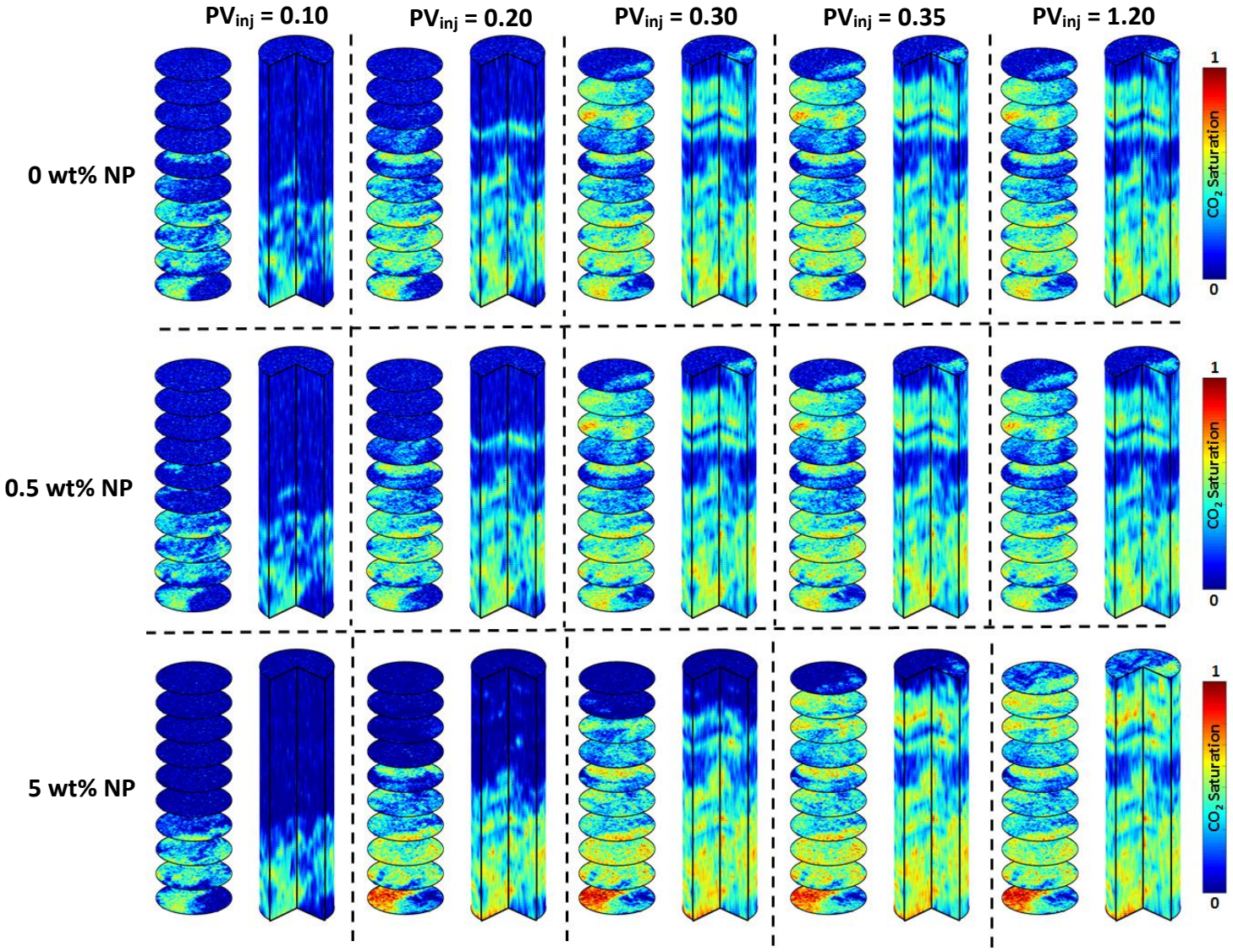

Figure 12. Distribution of CO_2 saturation during drainage experiments as computed by CT scanning.

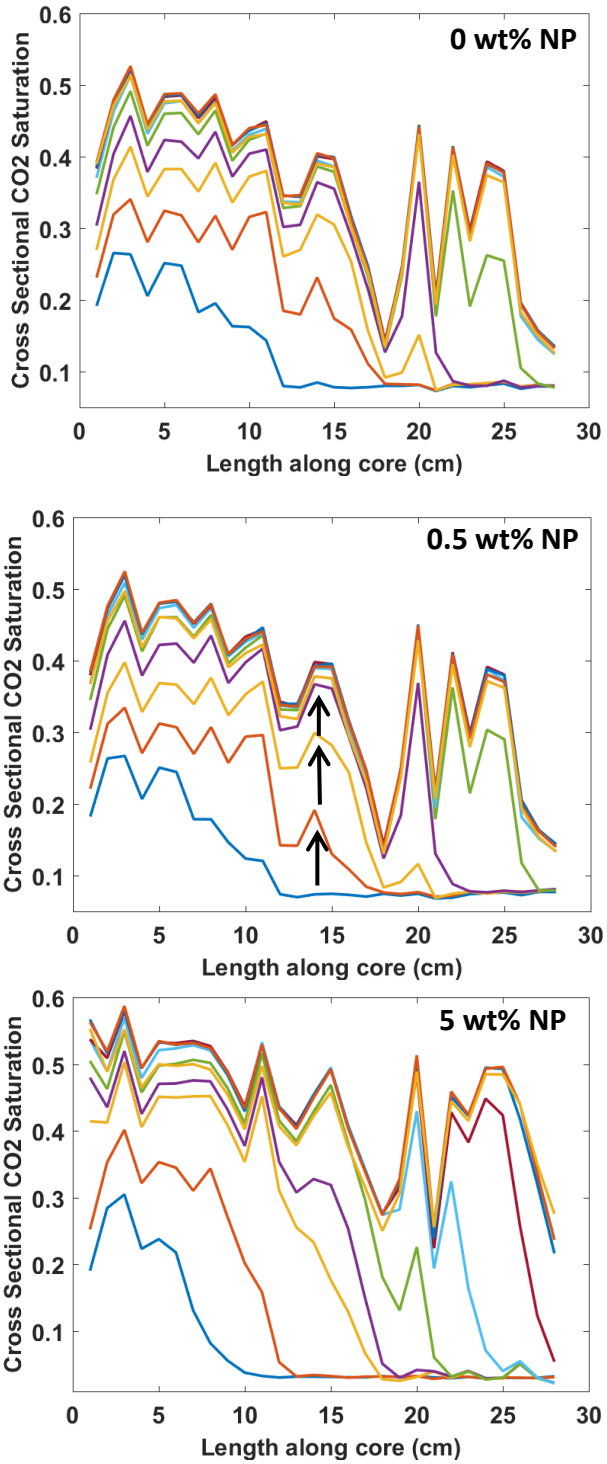

Figure 13. CT saturation profiles during drainage experiments.

Figure 13 shows the CO_2 saturation profiles within the core at PV_{inj} = 0.050, 0.100 … 0.400, 0.450, and 1.20. The saturations correspond to cross-sectional averages for each slice.

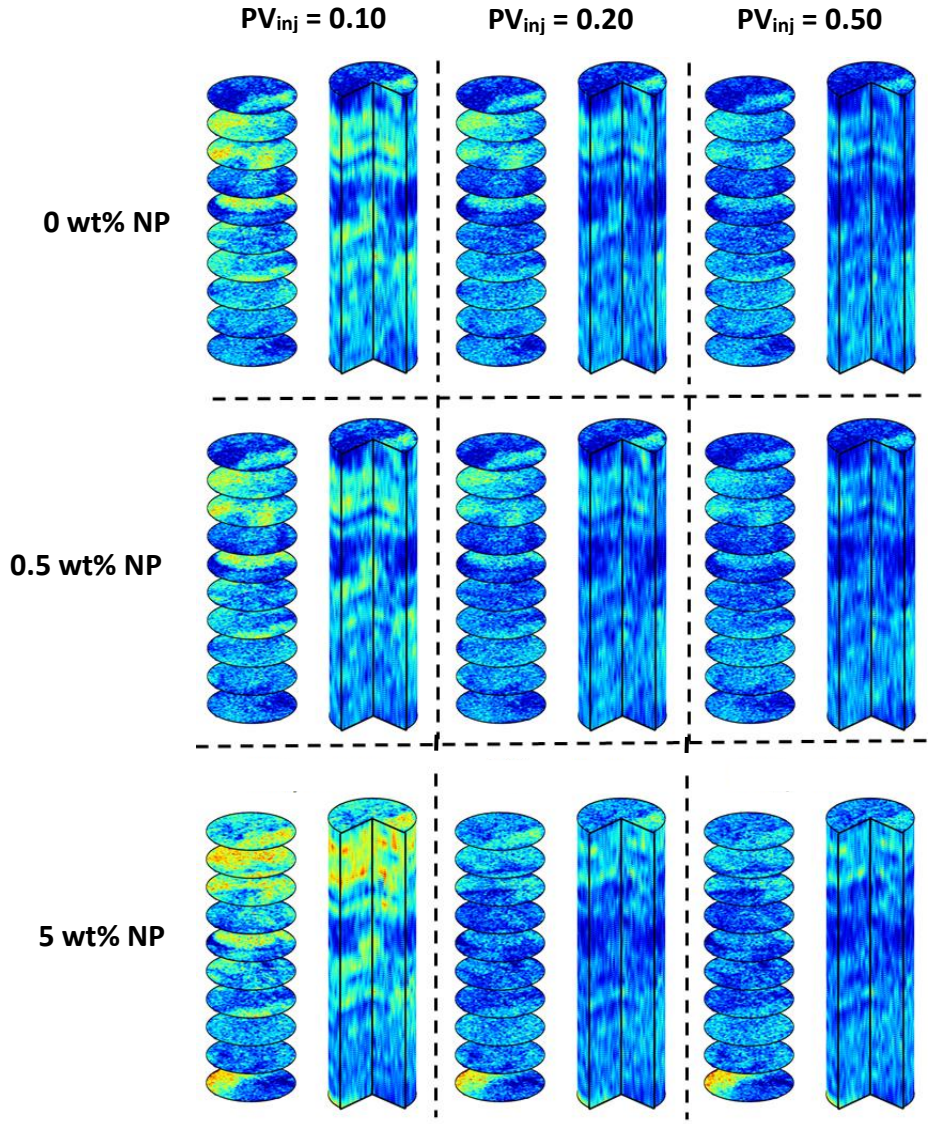

Figure 14. Distribution of CO_2 saturation during imbibition experiments as computed by CT scanning.

Figure 14 is similar to Figure 11, except it depicts the drainage process. All experiments reached steady-state by 0.50 PV of brine injected. CO_2 exits the core as brine is injected from the bottom.

2.4 Discussion

2.4.1 Relative Effectiveness of Nanoparticle Concentrations

The above results show that 0.5 wt% NP experiment only slightly improved the CO_2 conformance when compared to the control 0 wt% NP experiment. The 5 wt% NP experiment, however, did show marked improvements by all the metrics used in this study.

Figure 10 and Table 1 show that the 0 wt% NP and 0.5 wt% NP experiments had very similar breakthrough times, steady-state saturations, and residual saturations. For all NP concentrations, steady-state saturation was reached almost immediately upon breakthrough; the exception is the 0 wt% NP case, which showed a slight rarefaction. The 5 wt% NP experiment featured later breakthrough, higher steady-state CO_2 saturation, and higher residual CO_2 saturation. It should also be noted that the trapping ratio increased across all nanoparticle concentrations.

Figure 11 and Table 2 show a similar trend in pressure drop. Both the 0 wt% NP and 0.5 wt% NP experiments have comparable peak ΔP and residual ΔP, but those values are significantly higher for 5 wt% NP. Steady-state ΔP shows the opposite trend: as nanoparticle concentration increases, the steady-state ΔP decreases. This can be explained by the fact that relative permeability to CO_2 increases at higher CO_2 saturation, which was shown to be correlated with nanoparticle concentration.

CT data also shows no notable difference between 0 wt% NP and 0.5 wt% NP experiments with regards to patterns of spatial CO_2 distribution. However, the 5 wt% NP experiment is characterized by a) slower CO_2 movement through the core, b) greater CO_2 saturation within invaded zones, and c) larger invaded zones (resulting in higher sweep efficiency).

Lower CO_2 velocity leads to greater residence time of CO_2 within the core and delayed breakthrough. At $PV_{inj} = 0.20$, for example, it can be seen in Figure 12 that CO_2 has advanced beyond the 19 cm mark for the 0 and 0.5 wt% NP experiments, but remains behind the 16 cm mark for the 5 wt% NP experiment. It can also be seen that the 0 and 0.5 wt% NP experiments resulted in breakthrough around 0.30 PV, while the 5 wt% NP experiment doesn't appear to break through until significantly later.

In the regions of the core that were invaded by CO_2, the 5 wt% experiments showed a higher saturation. For the 0 and 0.5 wt% experiments at $PV_{inj} = 1.20$ (steady-state) and a depth of 1 cm (the bottom of the core), the bottom of the core is shaded yellow, indicating a saturation of approximately 50%. But the same region for the 5 wt% experiment is shaded red, indicating a CO_2 saturation in excess of 75%. This trend is observable in other regions of the core as well.

The invaded regions themselves are larger for the 5 wt% NP experiment, corresponding to a greater sweep efficiency. For example, at $PV_{inj} = 1.20$ at a depth of 19 cm (the 4th slice from the top) it can be seen that CO_2 invades regions of the core that are untouched in the 0 and 0.5 wt% NP experiments. Similarly, at the top of the column it can

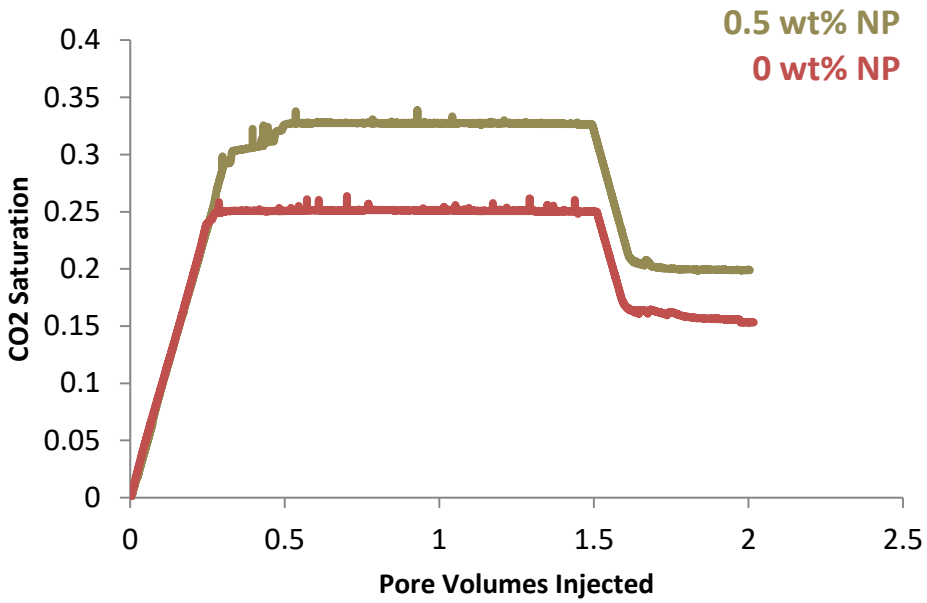

Figure 15. CO_2 saturation data for low flow rate (q = 0.8 cc/min) vertical corefloods from Wung (2015).

be seen that the 0 and 0.5 wt% NP experiments exited the core by forming a small thin filament while in the 5 wt% NP experiment the CO_2 exited in more of a plug- or shock-like fashion.

The shocks can be more clearly seen in Figure 13. The 5 wt% NP experiment forms steeper CO_2 saturation profiles; shallower profiles are seen for 0 and 0.5 wt% NP. Figure 13 also highlights the vertically homogenous nature of the core used in this experiment. The valleys in the saturation profiles indicate that the slices at 18cm and 21 cm store are less permeable to CO_2.

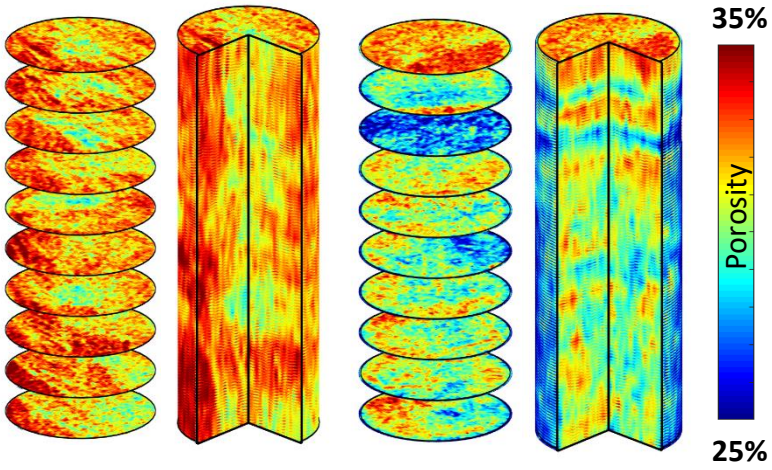

Figure 16. Porosity distribution for the cores used in Wung (2015) (left) and this study (right).

2.4.2 Effect of Bedding Layers and Pore-Scale Heterogeneity

Previous vertical corefloods with a low flow rate performed by Wung (2015) yielded different results (Figure 15). Wung found that there was a significant difference between 0 wt% and 0.5 wt% NP- close to a 30% improvement in steady-state CO_2 saturation and 33% improvement in residual CO_2 saturation. Our study showed almost no improvement, and it was not until NP concentration was increased to 5 wt% did steady-state and residual CO_2 saturation increase significantly. Wung did not test a 5 wt% NP concentration with a low flow rate, and Wung's flow rate was above the rate that would be estimated using the Buckley-Leverett approach.

A key difference between this study and that of Wung is the distribution of heterogeneities within the core. Figure 16 shows the porosity distribution of the cores used in Wung (2015) and in this study. The bedding layers of Wung's core run *parallel* to the

direction of flow, while the core used in this study features bedding layers oriented *perpendicular* to the direction of flow. The lowest-porosity bedding layers can be seen located at 21 cm and 23cm.

One interpretation of the heterogeneity information and experimental results is that bedding layers are far more effective at retarding CO_2 flow than nanoparticles.. This can be explained by considering the saturation profiles in Figure 13b. Concentration in the first 10 cm of the core increases at a roughly constant rate up the first 0.35 PV injected (until the purple curve). That purple curve represents the moment where CO_2 advanced beyond the tight, low-porosity region at 21 cm. The bedding layer serves as a bottleneck that, until crossed, forces the CO_2 fingers behind it to widen, which increases the sweep efficiency. Once the constriction is passed, CO_2 fingers stop widening and reach steady-state rapidly. This pattern can be seen in both 0 and 0.5 wt% NP experiments, indicating that the bedding layers play a more important role in controlling preferential flow paths than does a low nanoparticle concentration.

Alternatively, the distribution of pore-scale heterogeneities may actually emphasize the importance of nanoparticles in improving foam quality and stability. The pore sizes are generally larger and more broadly distributed in the core used by Wung and thus lower quality foam, stabilized only by 0.5 wt% NP, was sufficient to block those pores. In this study, the narrowly-distributed and generally lower porosity requires higher nanoparticles concentrations to effectively divert flow.

2.4.3 NANOPARTICLE-STABILIZED FOAM TRANSPORT DYNAMICS

Considerable work has been done on the mechanisms and factors that control foam transport in porous media (Zhang et al. 2009, Nguyen et al. 2000). Many of the models proposed to describe foam generation and transport propose that an interplay between bubble generation and bubble destruction/coalescence is what determines whether foams are stable. Kovscek (1993, 1995) proposed that bubble generation rate was proportional to the flowing foam velocity, and bubble destruction rate increased asymptotically as applied capillary pressure approached the critical capillary pressure (above which strong foams were not stable). Additionally, a minimum driving force is required to mobilize the foam, which can depend on pore geometry, foam texture, and matrix wettability (Rossen 1990).

All experiments, but 5 wt% NP in particular, show a rising ΔP corresponding to increasing accumulation of foam within the core before CO_2 breaks through. Following breakthrough, the ΔP starts to decrease, indicating that foam is being transported out of the core. It thus appears likely that even at the low velocities that characterize gravity-driven flow, there exists sufficient driving force to both generate and transport foams.

2.5 Summary of Chapter 2

One of the methods presented in Chapter 1 for producing buoyancy-driven flow, the rate-controlled Buckley-Leverett approach, was implemented in Chapter 2. Specifically, the possibility of using surface-coated silica nanoparticles to control the conformance of CO_2 moving only under the force of buoyancy was investigated. A cross-bedded sandstone core was saturated with brine/nanoparticle solution; the core was

oriented vertically within a modified medical CT scanner while a drainage experiment (CO2 injection) and imbibition experiment (subsequent brine injection) were conducted. CT scans were taken at regular intervals, which allowed *in-situ* flow patterns to be visualized.

Three nanoparticle concentrations tested were 5 wt%, 0.5 wt%, and 0 wt% (control). It was found that the addition of 0.5 wt% NPs did not improve conformance, as measured by saturation and pressure drop data, when compared to the control case. Adding 5 wt% of NPs proved to have a significantly larger effect. This result is at odds with those found in Wung (2015), where the addition of just 0.5 wt% NP caused significant conformance improvement. It is thought that much of this difference is due to the presence of cross-bedding and its orientation perpendicular to the direction of flow.

CHAPTER 3: CONCLUSIONS AND FUTURE WORK

The work done here has direct application to the study of buoyancy-driven flow and conformance control using surface-coated silica nanoparticles in porous media, specifically in the context of carbon sequestration.

3.1 Conclusions

Buoyancy-driven flow is an important phenomenon that occurs naturally (as in hydrocarbon migration) as well as in manmade contexts (as in carbon sequestration). There have been many attempts to study buoyancy-driven flow- many in the form of simulations or sand tank experiments. Although very useful, these methods are not able to faithfully recreate the subsurface conditions that would be present in deep-saline aquifers during CO_2 injection. High-pressure corefloods, if coupled with imaging technology like vertically oriented X-ray CT scanners, represent a quick, reproducible, and physically realistic alternative to study the multiphase flow behavior of buoyancy-driven CO_2 flow at aquifer conditions.

Little prior work was found on the subject of replicating the buoyancy-driven flow itself during high-pressure corefloods. Properly controlling the boundary conditions is crucial to accurately producing buoyancy-driven flow. Four different methods to do so were presented in Chapter 1- two pressure-controlled methods ("inject low and let rise" and progressive pressure increase) and two rate-controlled methods (simplified Darcy's Law, and the Buckley-Leverett approach).

The first pressure controlled method, "inject low and let rise," consists of injecting a set amount of CO_2 into the top of a vertical core, sealing the inlets, and then inverting the core. CO_2 then rises, driven only by its own buoyancy. Although methodologically

relatively simple, questions remain about the effect of countercurrent flow at the core-scale. In large aquifers, rising CO_2 may not require water to flow downwards at significant velocities, but in a relatively small, closed system (such as a core) the countercurrent water flow will likely affect the buoyant flow of the CO_2.

The progressive pressure increase method is experimentally analogous to invasion percolation simulations. It involves increasing the pressure of an upstream reservoir of CO_2 until CO_2 enters the core. The pressure is maintained until CO_2 ceases to flow into the core. The pressure is increased again and the process is repeated until CO_2 breaks through. This method, while relatively straight-forward to implement in simulations, could be very challenging to execute experimentally. It involves extremely fine control of core and pump pressures, which are unlikely to be achieved using traditional laboratory equipment such as nitrogen-charged back pressure regulators.

With rate-controlled corefloods, a buoyancy-driven flow rate is calculated for a given core and fluid system. Injecting CO_2 into a vertically oriented core at a rate below the buoyancy-driven flow rate is sufficient to achieve buoyancy-driven flow. These calculations make certain assumptions, such as CO_2 moving as a shock front. The Simplified Darcy's Law method additionally assumes that CO_2 behind the shock exists at $1 - S_{w,irr}$ (where $S_{w,irr}$ is the irreducible water saturation). The Buckley-Leverett approach instead determines the CO_2 shock saturation numerically.

The Buckley-Leverett approach was used to determine that the buoyancy-driven flow rate for a 30 cm long, 2.85 in diameter, 2.5 Darcy sandstone core was 0.30 mL/min. This flow rate was used in Chapter 2 to conduct a high-pressure vertical coreflood. Nanoparticles were placed into the core at several concentrations before the CO_2 injection to simulate an aquifer treated with nanoparticles to promote conformance control.

The control experiments (0 wt% NPs) showed a steady-state (drainage) saturation of 27% and residual (imbibition) saturation of 7%. These numbers were virtually unaffected by the addition of 0.5 wt% NPs, but at 5 wt% NPs steady-state saturation increased to 39% and residual saturation increased to 14%. Similarly, pressure drop data revealed that the residual pressure drop were similar for the 0 and 0.5 wt% nanoparticle experiments, but increased dramatically for the 5 wt% nanoparticle experiment.

These results stand in contrast with previous vertical core-flood experiments. Wung (2015) showed that the addition of 0.5 wt% did make a significant impact, as measured both by saturation and pressure data. Wung did not use the Buckley-Leverett approach to calculate the buoyancy-driven flow rate, and perhaps more importantly, Wung's core displayed a very different pattern of pore-scale heterogeneity. Wung's core featured bedding layers parallel to the direction of flow, while the bedding layers of this study's core ran perpendicular to the flow direction. This indicates that the effect of nanoparticles is attenuated in the presence of natural barriers to flow, such as low-porosity bedding layers.

There are indications that the flow rate determined using the Buckley-Leverett approach is suitable to replicate buoyancy-driven flow. Most notably, there is little to no rarefaction; the core reaches steady-state saturation just as it breaks through, which is a key characteristic of buoyancy-driven flow. However, the shock saturation/steady-state saturation predicted by the Buckley-Leverett approach was significantly lower than that observed in the experiment.

3.2 Future Work

It is common to run corefloods as rate-controlled experiments, but when modelling assumptions (like 1D flow) are not valid, it may be difficult to confidently predict the conditions required to recreate buoyancy-driven flow. In these cases, pressure controlled methods may be more suitable. The "inject low and let rise" method is relatively easy to implement. Countercurrent flow at the core scale must be considered, and should be viewed as an opportunity to perform novel research.

The experiments conducted in this study used liquid CO_2, but at aquifer temperatures CO_2 will exist in its supercritical form. Supercritical CO_2 has different physical and thermal properties than liquid CO_2, such as density and viscosity (Ouyang 2011). Conducting corefloods similar to the ones in this study, except at supercritical conditions (above 1071 psi and 31ºC), would most closely replicate the physical conditions found in the aquifer during CO_2 invasion (Harris and Yung 1995).

The placement of nanoparticles above a CO_2 sequestration target aquifer has been suggested (DiCarlo 2011) as a means to prevent leakage and unexpected CO_2 migration towards the surface. If CO_2 were to migrate, it would do so via the most permeable pathways, which are often fractures. Conducting similar experiments using fractured or mechanically compromised cores would shed light on the suitability of nanoparticles to prevent or slow leakage through fractures, rather than just improving the conformance of CO_2 travelling through the aquifer.

CO_2-in-water foams are thought to be formed during CO_2 injection into brine-saturated porous media. This study joins others in offering support to the idea that nanoparticles can stabilize those foams. Another additive used to stabilize foams are surfactants. There is evidence that combining both nanoparticles and surfactants can lead

to an additional synergy that results in higher foam stability (Worthen et al. 2013), the effect of which should be studied at the lab scale with coreflood experiments.

REFERENCES

Aminzadeh, B., Huh, C., Bryant, S. L., DiCarlo, D. A., & Roberts, M. (2012). Effect of nanoparticles on flow alteration during CO_2 injection. Presented at the *SPE Annual Technical Conference and Exhibition* at San Antonio, TX.

Andrew, J. C., Haszeldine, R. S., & Nazarian, B. (2015). The Sleipner CO_2 storage site: using a basin model to understand reservoir simulations of plume dynamics. *First Break*, *33*(6), 61-68.

Arts, R. J., Chadwick, A., Eiken, O., Thibeau, S., & Nooner, S. (2008). Ten years' experience of monitoring CO_2 injection in the Utsira Sand at Sleipner, offshore Norway. *First Break*, *26*(1).

Binks, B. P. (2002). Particles as surfactants—similarities and differences. *Current Opinion in Colloid & Interface Science*, 7(1), 21-41.

Brock, D. C., & Orr Jr, F. M. (1991). Flow visualization of viscous fingering in heterogeneous porous media.

Bryant, S. L., Lakshminarasimhan, S., & Pope, G. A. (2006). Buoyancy-dominated multiphase flow and its impact on geological sequestration of CO_2. Presented at the 2006 *SPE/DOE Symposium on Improved Oil Recovery* in Tulsa, OK.

Buckley, S. E., & Leverett, M. (1942). Mechanism of fluid displacement in sands. *Transactions of the AIME*, 146(01), 107-116.

Carrigan, C. R., Ramirez, A. L., Newmark, R. L., Aines, R., & Friedmann, S. J. (2009). *Application of ERT for tracking CO_2 plume growth and movement at the SECARB Cranfield site* (No. LLNL-CONF-412618). Lawrence Livermore National Laboratory (LLNL), Livermore, CA.

Carruthers, D. J., 2003, Modeling of secondary petroleum migration using invasion percolation techniques, in Duppenbecker, S. and Marzi, R., (Eds.), Multidimensional Basin Modeling, AAPG/Datapages Discovery Series No. 7, p 2137.

Catalan, L., Xiaowen, F., Chatzis, I., & Dullien, F. A. (1992). An experimental study of secondary oil migration (1). *AAPG Bulletin*, 76(5), 638-650.

Chen, X., Kianinejad, A., & DiCarlo, D. A. (2014). An experimental study of CO_2-brine relative permeability in sandstone. Presented at the 2014 SPE improved oil recovery symposium at Tulsa, OK.

Chou, S. I., Vasicek, S. L., Pisio, D. L., Jasek, D. E., & Goodgame, J. A. (1992). CO_2 foam field trial at north ward-estes. Presented at the 1992 SPE annual technical conference and exhibition in Washington, DC.

Chung, D. H. (2013). Transport of nanoparticles during drainage and imbibition displacements in porous media. University of Texas Petroleum and Geosystems Engineering Thesis Repository.

Derjaguin, B., & Landau, L. (1941). The theory of stability of highly charged lyophobic sols and coalescence of highly charged particles in electrolyte solutions. *Acta Physicochim. URSS*, 14(633-52), 58.

DiCarlo, D. A., Aminzadeh, B., Roberts, M., Chung, D. H., Bryant, S. L., & Huh, C. (2011). Mobility control through spontaneous formation of nanoparticle stabilized emulsions. *Geophysical Research Letters*, 38(24).

Doughty, C., & Pruess, K. (2004). Modeling supercritical carbon dioxide injection in heterogeneous porous media. *Vadose Zone Journal*, *3*(3), 837-847.

Duan, Z., & Sun, R. (2003). An improved model calculating CO 2 solubility in pure water and aqueous NaCl solutions from 273 to 533 K and from 0 to 2000 bar. Chemical geology, 193(3), 257-271.

Fagerlund, F., Illangasekare, T. H., & Niemi, A. (2007). Nonaqueous-phase liquid infiltration and immobilization in heterogeneous media: 1. Experimental methods and two-layered reference case. *Vadose Zone Journal*, *6*(3), 471-482.

Fernandez, J., Kurowski, P., Petitjeans, P., & Meiburg, E. (2002). Density-driven unstable flows of miscible fluids in a Hele-Shaw cell. *Journal of Fluid Mechanics*, *451*, 239-260.

Glass, R. J., Conrad, S. H., & Peplinski, W. (2000). Gravity-destabilized nonwetting phase invasion in macroheterogeneous porous media: Experimental observations of invasion dynamics and scale analysis. *Water Resources Research*, 36(11), 3121-3137.

Hansen, J., Sato, M., Kharecha, P., Beerling, D., Berner, R., Masson-Delmotte, V., Pagani, M., Raymo, M., Royer, D. L., & Zachos, J. C. (2008). Target Atmospheric CO_2: Where Should Humanity Aim? *The Open Atmospheric Science Journal*, 2(1), 217-231.

Harris, J. G., & Yung, K. H. (1995). Carbon dioxide's liquid-vapor coexistence curve and critical properties as predicted by a simple molecular model. *The Journal of Physical Chemistry*, *99*(31), 12021-12024.

Hirasaki, G. J., & Lawson, J. B. (1985). Mechanisms of foam flow in porous media: apparent viscosity in smooth capillaries. *Society of Petroleum Engineers Journal*, 25(02), 176-190.

Homsy, G. M. (1987). Viscous fingering in porous media. *Annual Review of Fluid Mechanics*, 19(1), 271-311.

Hovorka, S. D., Meckel, T. A., & Trevino, R. H. (2013). Monitoring a large-volume injection at Cranfield, Mississippi—Project design and recommendations. *International Journal of Greenhouse Gas Control*, *18*, 345-360.

Intergovernmental Panel on Climate Change. (2005). IPCC special report on carbon dioxide capture and storage. Prepared by Working Group III of the Intergovernmental Panel on Climate Change [Metz B, Davidson O, de Coninck H C, Loos M and Meyer L A (eds.)]. Cambridge University Press, New York.

Khatib, Z. I., Hirasaki, G. J., & Falls, A. H. (1988). Effects of capillary pressure on coalescence and phase mobilities in foams flowing through porous media. *SPE Reservoir Engineering*, 3(03), 919-926.

Kovscek, A. R., Patzek, T. W., & Radke, C. J. (1993). Simulation of foam transport in porous media. In *SPE Annual Technical Conference and Exhibition*. Society of Petroleum Engineers.

Kovscek, A. R., & Radke, C. J. (1994). Fundamentals of foam transport in porous media.

Krevor, S., Pini, R., Li, B., & Benson, S. M. (2011). Capillary heterogeneity trapping of CO_2 in a sandstone rock at reservoir conditions. *Geophysical Research Letters*, 38(15).

Krevor, S., Pini, R., Zuo, L., & Benson, S. M. (2012). Relative permeability and trapping of CO_2 and water in sandstone rocks at reservoir conditions. *Water Resources Research*, *48*(2).

Krishnamurthy, P. G., Senthilnathan, S., Yoon, H., Thomassen, D., Meckel, T., & DiCarlo, D. (2017). Comparison of Darcy's law and invasion percolation simulations with buoyancy-driven CO_2-brine multiphase flow in a heterogeneous sandstone core. *Journal of Petroleum Science and Engineering*, 155, 54-62.

Lake, Larry W. Enhanced Oil Recovery. Englewood Cliffs, N.J: Prentice Hall, 1989. Print.

Lee, J. (2007). Fluid Flow Through Permeable Media. In Lake, L. W. and Holsten, E. D. (Eds.), *Petroleum Engineering Handbook*, Volume 5, Richardson, TX: Society of Petroleum Engineers.

Lenormand, R., Touboul, E., & Zarcone, C. (1988). Numerical models and experiments on immiscible displacements in porous media. *Journal of Fluid Mechanics*, *189*, 165-187.

Li, H., Pan, C., & Miller, C. T. (2005). Pore-scale investigation of viscous coupling effects for two-phase flow in porous media. *Physical Review E, 72*(2), 026705.

Maxworthy, T. (1986). Bubble formation, motion and interaction in a Hele-Shaw cell. *Journal of Fluid Mechanics*, *173*, 95-114.

McNeil, B. I., & Matear, R. J. (2008). Southern Ocean acidification: A tipping point at 450-ppm atmospheric CO_2. *Proceedings of the National Academy of Sciences*, 105(48), 18860-18864.

Meckel, T. A., Bryant, S. L., & Ganesh, P. R. (2015). Characterization and prediction of CO_2 saturation resulting from modeling buoyant fluid migration in 2D heterogeneous geologic fabrics. *International Journal of Greenhouse Gas Control*, *34*, 85-96.

Nguyen, Q. P., Alexandrov, A. V., Zitha, P. L., & Currie, P. K. (2000). Experimental and modeling studies on foam in porous media: a review. In *SPE International Symposium on Formation Damage Control*. Society of Petroleum Engineers.

Nordbotten, J. M., Celia, M. A., & Bachu, S. (2005). Injection and storage of CO_2 in deep saline aquifers: analytical solution for CO_2 plume evolution during injection. *Transport in Porous media*, *58*(3), 339-360.

Ouyang, L. B. (2011). New correlations for predicting the density and viscosity of supercritical carbon dioxide under conditions expected in carbon capture and sequestration operations. *Open Petroleum Engineering Journal*, *5*(1), 13-21.

Pickering, S. U. (1907). CSCVI- Emulsions. *Journal of the Chemical Society Transactions*, 91, 2001-2021.

Prodanovic, M., Ryoo, S., Rahmani, A. R., Kuranov, R. V., Kotsmar, C., Milner, T. E., Johnston, K. P., Bryant, S. L. & Huh, C. (2010). Effects of magnetic field on the motion of multiphase fluids containing paramagnetic nanoparticles in porous media. Presented at the 2010 SPE Improved Oil Recovery Symposium.

Purcell, W. R. (1949). Capillary pressures-their measurement using mercury and the calculation of permeability therefrom. *Journal of Petroleum Technology*, *1*(02), 39-48.

Ramsden, W. (1903). Separation of solids in the surface-layers of solutions and suspensions- observations on surface-membranes, bubbles, emulsions, and mechanical coagulation)- preliminary account. *Proceedings of the Royal Society of London*, 72, 156-164.

Roof, J. G. (1970). Snap-off of oil droplets in water-wet pores. *Society of Petroleum Engineers Journal*, 10(01), 85-90.

Rossen, W. R. (1990). Theory of mobilization pressure gradient of flowing foams in porous media: I. Incompressible foam. *Journal of Colloid and Interface Science, 136*(1), 1-16.

Saadatpoor, E., Bryant, S. L., & Sepehrnoori, K. (2010). New trapping mechanism in carbon sequestration. *Transport in Porous Media*, *82*(1), 3-17.

Saffman, P. G., & Taylor, G. (1958). The penetration of a fluid into a porous medium or Hele-Shaw cell containing a more viscous liquid. In *Proceedings of the Royal Society of London A: Mathematical, Physical and Engineering Sciences* (Vol. 245, No. 1242, pp. 312-329). The Royal Society.

Saripalli, P., & McGrail, P. (2002). Semi-analytical approaches to modeling deep well injection of CO_2 for geological sequestration. *Energy Conversion and Management*, *43*(2), 185-198.

Tambe, D. E., & Sharma, M. M. (1994). The effect of colloidal particles on fluid-fluid interfacial properties and emulsion stability. *Advances in Colloid and Interface Science*, 52, 1-63.

Trevisan, L., Pini, R., Cihan, A., Birkholzer, J. T., Zhou, Q., & Illangasekare, T. H. (2015). Experimental analysis of spatial correlation effects on capillary trapping of supercritical CO_2 at the intermediate laboratory scale in heterogeneous porous media. *Water Resources Research*, 51(11), 8791-8805.

Trevisan, L., Pini, R., Cihan, A., Birkholzer, J. T., Zhou, Q., & Illangasekare, T. H. (2014). Experimental investigation of supercritical CO_2 trapping mechanisms at the intermediate laboratory scale in well-defined heterogeneous porous media. *Energy Procedia*, *63*, 5646-5653.

Wellington, S. L., & Vinegar, H. J. (1985). CT studies of surfactant-induced CO_2 mobility control. Presented at the 1985 *SPE Annual Technical Conference and Exhibition* in Las Vegas, NV.

Wilkinson, D., & Willemsen, J. F. (1983). Invasion percolation: a new form of percolation theory. *Journal of Physics A: Mathematical and General*, 16(14), 3365.

Worthen, A. J., Bryant, S. L., Huh, C., & Johnston, K. P. (2013). Carbon dioxide-in-water foams stabilized with nanoparticles and surfactant acting in synergy. *AIChE Journal*, *59*(9), 3490-3501.

Wung, R. M. (2015). Utilizing Surface Treated Nanoparticles for Enhanced Geologic Carbon Sequestration. University of Texas Petroleum and Geosystems Engineering Thesis Repository.

Yu, J., An, C., Mo, D., Liu, N., & Lee, R. L. (2012). Foam mobility control for nanoparticle-stabilized supercritical CO_2 foam. Presented at the 2012 SPE Improved Oil Recovery Symposium in Tulsa, OK.

Zhang, C., Oostrom, M., Grate, J. W., Wietsma, T. W., & Warner, M. G. (2011). Liquid CO_2 displacement of water in a dual-permeability pore network micromodel. *Environmental Science & Technology*, *45*(17), 7581-7588.

Zhang, T., Roberts, M., Bryant, S. L., & Huh, C. (2009). Foams and emulsions stabilized with nanoparticles for potential conformance control applications. Presented at the 2009 SPE International Symposium on Oilfield Chemistry at The Woodlands, TX.

ssenthil@utexas.edu

This thesis was typed by Siddharth Senthilnathan.